

Adaptable Microfluidic Vessel-on-a-Chip Platform for Investigating Tumor Metastatic Transport in Bloodstream

Yue Wu, Yuyuan Zhou, Ratul Paul, Xiaochen Qin, Khayrul Islam, and Yaling Liu*



Cite This: *Anal. Chem.* 2022, 94, 12159–12166



Read Online

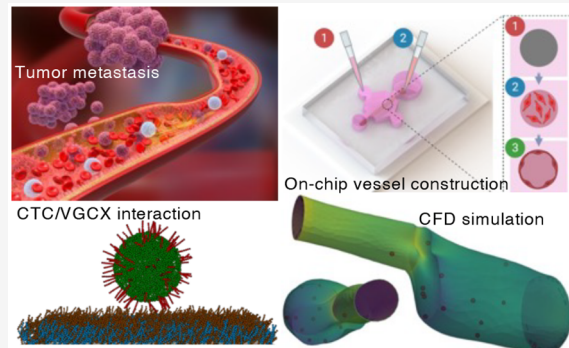
ACCESS |

Metrics & More

Article Recommendations

Supporting Information

ABSTRACT: Cancer metastasis counts for 90% of cancer fatalities, and its development process is still a mystery. The dynamic process of tumor metastatic transport in the blood vessel is not well understood, in which some biomechanical factors, such as shear stress and various flow patterns, may have significant impacts. Here, we report a microfluidic vessel-on-a-chip platform for recapitulating several key metastatic steps of tumor cells in blood vessels on the same chip, including intravasation, circulating tumor cell (CTC) vascular adhesion, and extravasation. Due to its excellent adaptability, our system can reproduce various microenvironments to investigate the specific interactions between CTCs and blood vessels. On the basis of this platform, effects of important biomechanical factors on CTC adhesion such as vascular surface properties and vessel geometry-dependent hemodynamics were specifically inspected. We demonstrated that CTC adhesion is more likely to occur under certain mechano-physiological situations, such as vessels with vascular glycocalyx (VGCX) shedding and hemodynamic disturbances. Finally, computational models of both the fluidic dynamics in vessels and CTC adhesion were established based on the confocal scanned 3D images. The modeling results are believed to provide insights into exploring tumor metastasis progression and inspire new ideas for anticancer therapy development.



Cancer is one of the greatest threats to human health today, and tumor metastasis is responsible for the vast majority of cancer deaths.¹ However, current understanding on cancer metastasis is still limited. While circulating tumor cells (CTCs) and circulating tumor cell clusters can be isolated from patient blood samples, how they originate and where they are going to end up remains as a mystery.² As it is a rare event, real-time tracking of metastatic processes *in vivo* is impossible.^{3,4} Model organisms, such as zebrafish, have been used to establish *in vitro* models of cancer metastasis.⁵ Nevertheless, such animal experiments are not only time consuming and costly, but the results are also far from predicting metastatic behavior in humans. Today, the increasingly advanced organ-on-a-chip technology makes it possible to accurately replicate specific pathological tissue models *in vitro*.^{6–11} Among them, the microfluidic vessel–tumor model has made important contributions to exploring the mechanism of cancer metastasis.^{12–18} In addition to being an important component of the tumor microenvironment, the blood vessel is also a highway for CTCs to escape and disseminate to distant organs. Notably, it has been gradually recognized that vascular-related biomechanical factors also play a nonignorable role in cancer metastasis¹⁹ (Figure 1A). The vascular flow pattern not only can act on the endothelium,²⁰ triggering a series of biochemical reactions,²¹ but also directly affect the physiological states of flowing CTCs,²² thereby affecting the outcome of cancer metastasis.²³ Practical and flexible microfluidic vessel–tumor

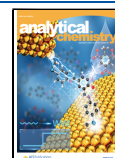
models are still urgently needed for this kind of fundamental research.

Here, we developed an adaptable vessel-on-a-chip platform to investigate how a range of mechano-physiological factors influence the CTCs metastatic transport in the bloodstream. By rebuilding different CTC–vessel interactions, the key steps involved in cancer metastasis are mimicked *in vitro*, including intravasation, CTC vascular adhesion, and extravasation. We demonstrated that both vascular glycocalyx (VGCX) shedding and vessel geometry-dependent hemodynamics can directly increase the probability of CTC vascular adhesion. In addition, computational models were established to interpret the fluid dynamics involved in CTC adhesion, and the simulation results were consistent with the experimental data. Such an adaptable vessel-on-a-chip platform is expected to advance the understanding of cancer metastasis progression and facilitate the development of new anticancer therapeutics.

Received: June 14, 2022

Accepted: August 12, 2022

Published: August 23, 2022



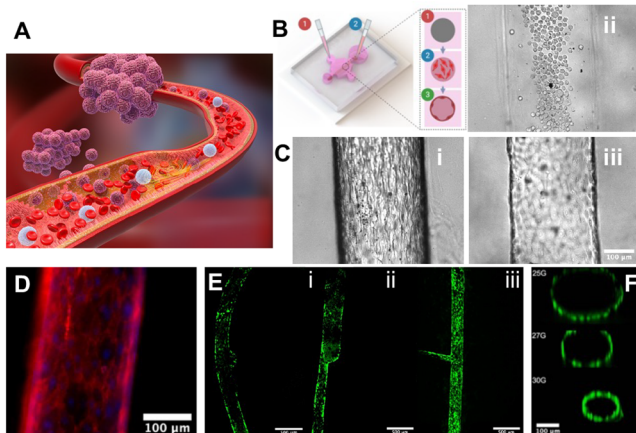


Figure 1. Schematic of methodology and construction of adaptable microfluidic on-chip vessel modeling. (A) Schematic showing vascular metastatic transport of CTCs. (B) Illustration of key steps of on-chip vessel biofabrication. (C) Brightfield microscopy of on-chip vessel construction process, including (i) rod embedding, (ii) endothelial cell (EC) seeding, and (iii) channel endothelialization. (D) CD31 immunostaining of the on-chip vessel model. DAPI signal (blue) stains cell nuclei. CD31 (orange) is clearly visible as the biomarker of the vessel. (E) Representative fluorescent (green) images of vessels with various geometries: (i) aneurysm, (ii) stenosis, and (iii) bifurcation are very common vessel geometries to induce disturbed flow. (F) Diameter control of the adaptable on-chip vessel modeling. Confocal scanning of vessels with diameters of 300, 210, and 160 μm , top to bottom. ECs were labeled with FITC.

■ EXPERIMENTAL SECTION

A hexagonal microfluidic chamber was designed to increase the contact area between the hydrogel and chamber to prevent collapse and fabricated using standard soft lithography techniques.^{24,25} Polydimethylsiloxane (PDMS) (SYL-GARD184, Dow Corning) rods were cast from hypodermic needles (Fisher Scientific, Pittsburgh, PA).²⁶ The fibrinogen pregel solution was mixed with 5U/mL of bovine thrombin (CAS-9002-044, Sigma) and injected into the chamber through the side loading ports. After 1 h of polymerization in the incubator, the PDMS rod was extracted, and the HUVEC suspension (8 million/mL) was seeded into the formed tubular channel. The confluent 3D on-chip vessel tube could be formed after 24 h incubation. As for the diffusion assay, the permeabilities of the vessels in different culture conditions were assessed by measuring solute diffusion across the vessel wall. Here, 70 kDa FITC-conjugated dextran (CAS-60842-46-8, Sigma) was dissolved in the EGM-2 medium to prepare a 25 $\mu\text{g}/\text{mL}$ solution. Then, 5 μL of the dextran solution was loaded into each vessel lumen, and the dextran diffusion was imaged with a Nikon Eclipse TE2000 inverted fluorescence microscope over 10 min.

Neuraminidase (Neur) enzyme was used for VGCX degradation, and wheat germ agglutinin (WGA) lectin was used for VGCX characterization. Recombinant human vascular endothelial growth factor (VEGF) 165A was used for angiogenic sprouting, and hepatocyte growth factor (HGF) was utilized for attracting tumor cells migration.^{27,28} The growth factor would gradually spread into the surrounding matrix and induce tumor cells to intravasate into the vessel.

For CTCs transport in the vessels of different conditions, the PC3 cells were resuspended in EGM-2 medium (0.5 million/mL) and perfused through the vessel at a flow rate of 5 $\mu\text{L}/\text{min}$

for half an hour. After perfusion, the attachment results of CTCs on vessels were imaged using the fluorescent microscope. All the fluorescent images and confocal scanning were acquired with a Nikon C2+ laser scanning confocal microscope in the Health Research Hub Center, Lehigh University. The image processing was conducted with ImageJ software from the National Institutes of Health (USA).

For computational fluid dynamics (CFD), the 3D model of the stenosis vessel was reconstructed by finding the edges of the cross-sectional slices taken from the confocal images by applying thresholding. The edges were traced in Solidworks 2021 to generate the 3D model. An Ansys Workbench 2021 (ANSYS, Inc.) was used for geometry discretization. Simulations were conducted in 3D and under steady-state conditions, considering an incompressible Newtonian flow. The Navier–Stokes equations were solved using the pressure–velocity coupling SIMPLE (semi-implicit method for pressure linked equations) method with second-order accuracy. Detailed experiments can be found in the Supporting Information.

■ RESULTS AND DISCUSSION

On-Chip Construction of Vessel Model and Dynamic Vessel–Microenvironment Interactions. Our platform provides a facile method to construct blood vessels and associated vascular microenvironments. After extraction of the cylindrical polydimethylsiloxane (PDMS) rod, a hollow channel was constructed inside of the fibrin gel (Figure 1B). A human umbilical vein endothelial cell (HUVEC) suspension of high concentration was loaded into the channel, and cells would cover the whole inner surface of the channel to form a confluent endothelialized lumen in 1 day (Figure 1C). The platelet endothelial cell adhesion molecule-1 (PECAM-1 or CD31) antibody was used to characterize the CD31 expression on each single HUVEC surface. The immunofluorescence result (Figure 1D) demonstrated the presence of CD31 and marked the formation of an intact endothelial lumen. From a hemodynamic point of view, the shapes and diameters of blood vessels are two direct factors that affect the flow pattern. The hemodynamic characteristics of different flows can directly influence the transport of CTCs, affecting their dissemination and colonization.²⁹ Limited by poor elasticity and difficulty in processing, a commonly used iron needle was used to make simple straight vessel lumens, which can only produce laminar flow inside.³⁰ By assembling various ductile PDMS rods together, structures of different shapes can be created in a controlled and repeatable manner. For example, to construct an on-chip stenotic vessel, a large rod cast from a 23-gauge needle and a small rod cast from a 30-gauge needle were vertically glued together with a PDMS presolution, prior to embedding into the gel. Thus, perfusable vessel lumens with different geometries, including aneurysms, stenosis, and bifurcations, can be constructed on-chip (Figure 1E, F).

Besides the adjustable vessel morphology, the adaptability of our vessel-on-a-chip platform was also demonstrated in construction of flexible vascular microenvironments. Distinct microenvironments were constructed to initiate the interactions, and the corresponding changes of the vessel physical profile were examined. In particular, two groups of vessels were cultured in prostate cancer cells PC3 cancer cells/normal human lung fibroblast (NHLF)-associated microenvironments, respectively, and a group of monocultured vessels served as the control. The vascular morphological changes were continuously recorded, and vascular barrier function was quantified by

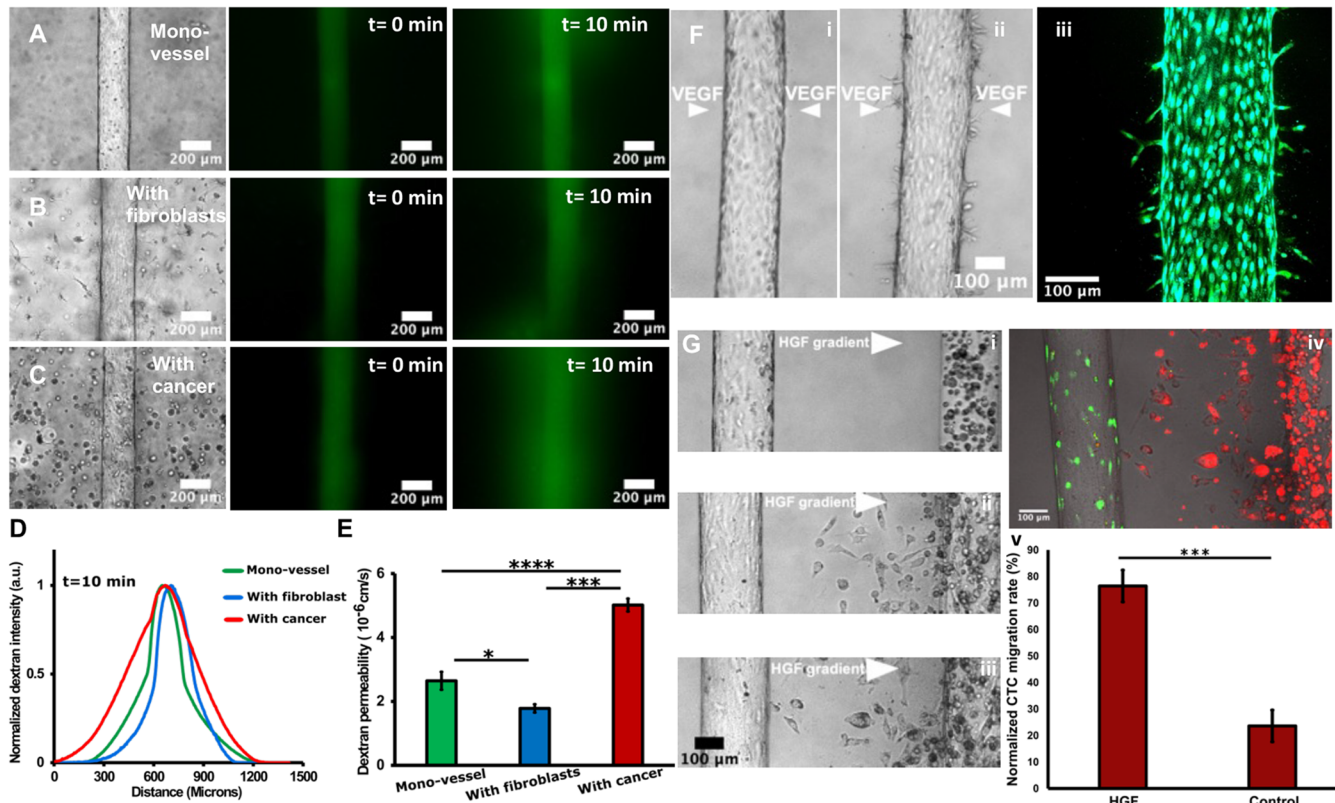


Figure 2. Dynamic interactions between vessels and various microenvironments. (A–C) Vessel permeabilities in monovessel culture, vessel–fibroblasts coculture, and vessel–cancer cells coculture. Representative fluorescent images at $t = 0$ min and $t = 10$ min, for diffusion of 70 kDa dextran in a monovessel (A), fibroblast-associated vessel (B), and cancer-associated vessel (C). (D) 70 kDa dextran diffusion profiles at $t = 10$ min for vessels in various culture conditions. (E) 70 Kda dextran permeability values calculated for vessels in various culture conditions. The cancer-associated vessels were the leakiest, while the fibroblast-associated microenvironments improved the barrier functions of the vessels, compared with the monocultured vessels. Three individual vessels ($n = 3$) were measured for each culture condition to determine the average permeability value: * $p < 0.05$, ** $p < 0.01$, *** $p < 0.001$, and **** $p < 0.0001$. (F) 3D angiogenesis in the adaptable vessel-on-a-chip platform: (i, ii) Newly sprouting microvessels can be induced from the primary vessel by a vascular endothelial growth factor (VEGF) in 2 days. (iii) Fluorescent microscopy of the angiogenetic sprouting vessels. HUVECs were stained with CellTracker green, and DAPI (blue) stains the nucleus. (G) On-chip modeling intravasation of PC3 clusters from the nearby matrix into the vessel tube. HGF-supplemented medium was perfused in the vessel, and a HGF gradience was formed in the local microenvironment. The PC3 cells were induced to migrate out of the clusters (i, ii) and intravasated to the vessel (iii) in response of the HGF gradience in 2 days. (iv) Fluorescent image of PC3 cancer cells (red) intravasating the vessel (green). (v) Normalized percentage of PC3 cell migrated from the surrounding collagen toward the vessel tube with/without of HGF stimulation.

measuring diffusion of a 70 kDa dextran solute on day 3 (Figure 2A–C). When grown alone, every endothelial cell on the vessel was in an oval shape with no observable differences appearing during a 3 day culture. While in the fibroblast-associated microenvironment, the endothelial cells appeared to be stretched into filaments and were more tightly connected to each other. However, the cancer-associated microenvironment turned the cells into a long strip shape, and the vessel looked fluffier. The morphological changes of the blood vessels are supposed to be closely related to their function alterations. To further test the vascular barrier function, we perfused the 70 kDa fluorescently conjugated dextran solution and tracked its diffusion cross vessel lumen over 10 min. The vessel in the cancer-associated microenvironment was the leakiest, and the dextran spread over twice the area of the one in the monocultured vessel (Figure 2D). The vascular permeability coefficient was also calculated for all three types of vessels (Figure 2E). The vessel permeability in the fibroblast microenvironment was slightly lower than that of the monocultured vessel and less than half of that in the cancer-associated microenvironment. In summary, the vascular barrier

function was enhanced in the fibroblast-associated microenvironment and downgraded in the cancer-associated microenvironment, thus reflecting the dynamic interactions between blood vessels and microenvironments. Figure 2F shows that a microenvironment containing a VEGF gradient can directly trigger the sprouting tips out of the primary vessel, which recapitulates the *in vivo* angiogenesis phenomenon. It is shown that vessel morphology can adapt to the local microenvironment, thereby affecting its function.

Modeling CTCs Intravasation into the Bloodstream. As one of the crucial steps of metastasis initiation, intravasation refers to how the CTCs enter into the bloodstream.³¹ After the formation of confluent vessel lumen, a PC3 cluster was seeded nearby to mimic the primary tumor. Then, the HGF-supplemented medium was perfused through the vessel to activate the tumor cell migration. HGF is a commonly used chemoattractant to stimulate tumor cells.³² It was observed that a few cells were gradually released from the primary tumor cluster and migrated toward the vessel (Figure 2G). After 2 days of migration, some tumor cells successfully penetrated the vessel wall and reached the vessel's inner surface and may

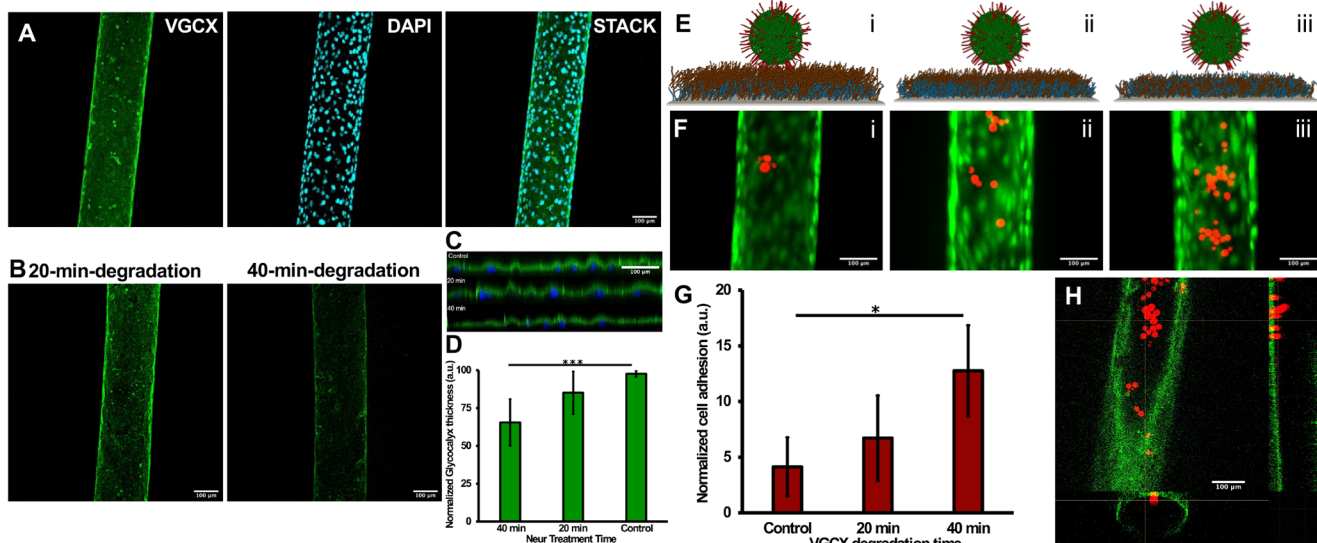


Figure 3. CTC adhesion result on vessels of different VGCX conditions. (A) Fluorescent staining of VGCX (green). DAPI signal (blue) stains cell nuclei. (B, C) VGCX was degraded by enzyme in a time dependent manner. After 20/40 min of enzyme degradation, the coverage and thickness of VGCX gradually decreased. (D) Data quantification for VGCX thickness change after different degradation treatments. Three individual samples were measured for each condition to determine the average value. Statistical significance between groups is denoted as * $P < 0.05$ and *** $P < 0.001$. (E) Schematics of the interactions between CTC and VGCX of different thicknesses: normal (i), 20 min degradation (ii), and 40 min degradation (iii). The red ligand stands for the glycocalyx structure. (F) Representative fluorescent images of adhered CTCs on normal vessel (i), vessel after 20 min VGCX degradation treatment (ii), and vessel after 40 min VGCX degradation treatment (iii). Vessels were stained with CellTracker green, and CTCs were stained with CellTracker red. (G) Normalized rate of adherence of CTCs on vessels with different VGCX degradation treatments. (H) Confocal scanning of adhered CTCs on VGCX. VGCX were labeled with WGA (FITC).

potentially become CTCs. In the control group, an HGF-free medium was perfused through the vessel. In that case, the tumor cells looked calmer, and most of them only proliferated *in situ* and did not migrate around (Figure 2G(v)). Our observation showed that abnormal concentrations of growth factors in the bloodstream may also lead to specific migratory responses of tumor cells. Silvestri et al. reported that a tumor organoid could make direct contact with blood vessels to make them part of themselves, while some small CTC clusters were peeled off and entered the blood flow.¹⁵ The metastasis could be a result of the systemic effect, rather than a single factor. A diseased *in vivo* environment may also lead to abnormalities in the endocrine system that promote CTCs disseminations.

Characterization of VGCX of the Vessel and Results of CTC Adhesion on VGCX Layers under Different States. Tumor necrosis factor- α (TNF- α)-related changes in cell adhesion have already been well studied.^{33,34} Relatively, VGCX, known as a mechano-transducer, tends to receive less attention.³⁵ As the first structure on the endothelium to be in contact with blood flow and floating cells, the VGCX covers various adhesion receptors such as integrins, immunoglobulins, and selectins.³⁶ By interacting with blood flow in different states, corresponding feedbacks will appear on its composition, thereby affecting receptor-mediated CTC–vascular adhesion. Here, as one of the research objects, the influence of VGCX coverage on CTC vascular adhesion was quantitatively studied. First, the VGCX was visualized by labeling it with FITC-fluorescent-conjugated WGA, which primarily marks the sialic acid (SA) component of VGCX. The WGA-labeled VGCX appeared as a uniform layer with no visible gaps between each endothelial cell (Figure 3A). Subsequently, the vessels were treated with a VGCX degradative enzyme, neuraminidase (Neur),³⁷ in a time-dependent manner. A group of nontreated

vessels were set as the control, and the other sets of samples were processed for 20 min, 40 min, and 1 h, respectively. The viability and integrity of the 1 h-treated group had been irreversibly damaged and were therefore not used for further study (Figure S1). The confocal scanning showed that the coverage of VGCX decreased with the increased enzyme treatment time (Figure 3B, C). After 40 min of treatment, the thickness of VGCX was just over 60% of that of the control group (Figure 3D).

Second, the model CTCs were perfused through the vessels of different VGCX statuses at 1 dyn/cm² for half an hour to measure the impact of VGCX on CTC adhesion. After perfusion, unadhered CTCs were slightly washed away, and the number of the attached CTCs was counted and normalized. Figure 3F reports representative fluorescent images showing the CTC adhesion results on the vessels of different VGCX statuses. The number of CTCs adhered on the normal vessel was the least, while that on the 40 min degradation vessel was the highest, almost three times that of the former (Figure 3G). A possible explanation is that the thinner the VGCX layer is, the greater the chance of exposure of various adhesion receptors and the greater the likelihood of bonding to CTC surface proteins, as illustrated in Figure 3E. Hynes et al. suggested that the endothelium itself exhibits an antifouling effect, which prevents the majority of CTC attachments compared to the bare ECM wall. Nevertheless, the role of blood vessels in this regard may also be related to its own state.³⁸ The healthy VGCX and diseased VGCX could have obviously different affinities for the contacting CTCs. *In vivo*, the VGCX shedding may be caused by both biochemical transitions (such as inflammation-induced protease secretion)³⁹ and abnormal physiological flow conditions.⁴⁰ Therefore, the influence of the local microenvironment may also

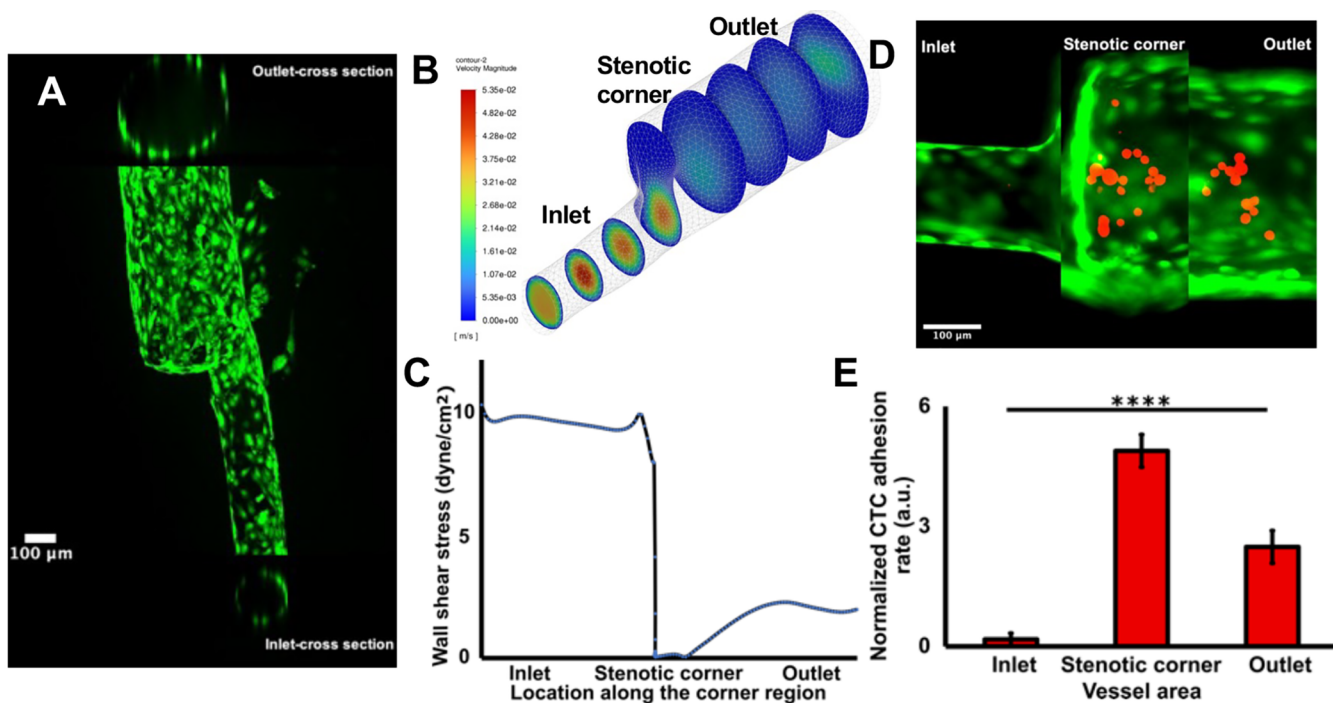


Figure 4. Analysis of CTC adhesion results along the stenotic vessel lumen. (A) Confocal scanning of the on-chip stenotic vessel model. HUVECs are stained with CellTracker green. (B) Fluid dynamic simulation of cell culture media perfusion presenting the velocity profile along the stenotic vessel lumen. Velocity profile at an inlet wall shear stress of 10 dyn cm^{-2} . (C) Flow wall shear stress distribution along the stenotic vessel direction. CTCs are perfused through on-chip of the stenotic vessel lumen. (D) Representative fluorescent images show the CTC adhesion result in the stenotic vessel lumen. The CTCs were stained with CellTracker red. (E) Normalized rate of CTC adhesion in the different regions of the stenotic vessel.

need to be comprehensively considered when studying the interaction of blood vessels and CTCs.

On-Chip Stenotic Vessel Construction and Characterization of CTC Adhesion Induced by Hemodynamic Flow Disturbance. In addition to the physiological structures on the blood vessels, hemodynamics can also affect the vascular transport and adhesion of CTCs. Here, we chose the stenotic vessel model as the subject to investigate how the vessel geometry-dependent hemodynamics affects CTC adhesion. A stenotic vessel lumen (about 160 μm for inlet diameter and 350 μm for outlet diameter) was constructed on-chip (Figure 4A). To further analyze the hemodynamics inside the stenotic vessel, a 3D model was reconstructed from the confocal scanning images and utilized for a computational fluid dynamics simulation. The velocity profile (Figure 4B) and shear stress (Figure 4C) at different sections of the vessel lumen were analyzed at an inlet wall shear stress (WSS) of 10 dyn/cm^2 . A small vortex was observed in the stenotic corner, and its area is related to flow rate and vessel geometry (Figure S3).⁴¹ Similarly, the CTCs suspension was perfused through the inlet for half an hour. Since the vessel diameter at the outlet zone was almost twice that of the inlet, the WSS at the outlet was only one tenth of that at the inlet.⁴² Figure S3B shows the CTCs motion along the stenotic vessel lumen. Around the stenotic corner, the flow regime suddenly changed from a stable laminar flow to a disturbed flow, and the velocity and WSS also dropped sharply (Figure 4D). Consequently, some CTCs were able to contact, roll, and adhere on the inner surface of the vessel. The number of adhered CTCs on different sections of the vessel after perfusion was counted and normalized. High WSS not only increases the rolling speed of

CTCs but also reduces the chance of CTCs contacting vessel walls. This may explain why there were few CTC adhesions in the high WSS inlet zone. In addition, the most CTC adhesion was found in the stenotic corner region, which coincided with the region with a sudden WSS drop. In the wide outlet vessel lumen, the flow pattern gradually recovered to a stable laminar flow with slow flow velocity, and the CTC adhesion rate was half of that in the corner region. Thus, it is assumed that a disturbed flow-associated vortex may reduce the local flow velocity, therefore increasing the probability of CTC contact and adhesion on the vessel surface in long-term perfusion. Chen et al. reported that the cramped capillary vessel tube could directly entrap the CTCs and induce transvascular migration of the trapped CTCs.⁴³ Our result shows that in addition to the physical structure capture effect, the vessel geometry induced flow biomechanics can also impact CTC adhesion.

Computational Modeling of CTC Adhesion under Different Vessel Conditions. To better understand the process and fluid dynamics involved in the CTC adhesion process, computational models were developed based on vessel geometry reconstructed from 3D scanned images. Figure 5 shows the simulation setup and CTC adhesion results. To visualize the WSS and locations of attached CTCs, the computational fluid dynamics simulation data are exported into Paraview for postprocessing.⁴⁴ At first, the CTC adhesions in the normal straight vessel lumen with different VGCX statuses were simulated. The vessels have cylindrical shapes under stable laminar flow with a no-slip boundary condition at the wall. A parabolic velocity profile is observed in the vessel. The simulations were running for 30 min. Since the exposed

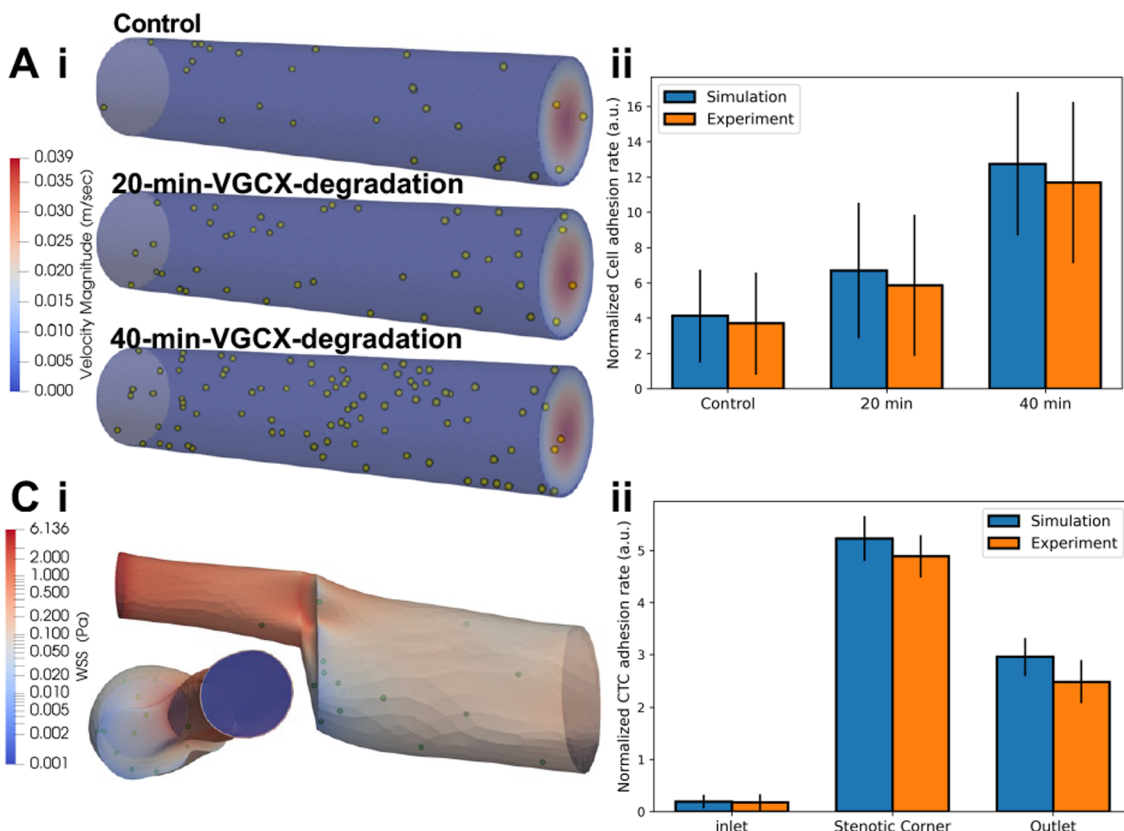


Figure 5. Computational CTC transport and adhesion modeling in different scenarios. (A) Modeling CTC adhesion in the normal vessel: (i) Simulated CTC adhesion result according to different VGCX layers. (ii) Comparison of simulation result with experimental result. (B) Modeling CTC adhesion in the stenotic vessel lumen: (i) Variation of WSS in the vessel domain and the CTC adhesion result. (ii) Comparison of simulation result with experimental result.

receptor level under different Neur treatment is unknown, the ligand–receptor density is parametrized by an empirical method to predict CTC attachment on the vascular wall. A receptor density of around 1.59 times under a 20 min treatment and around 1.75 times under a 40 min treatment compared to healthy VGCX lumen were found to match with the experimental values of CTC adhesion density. The computational model had a good qualitative agreement with the experimental data (Figure 5A(ii)), but there is a quantitative discrepancy between the experimental and simulated results. In the experiment, attachment of CTCs as clusters is observed, where CTCs in the computational model are treated independently without cell–cell interactions considered.

The same model is used to simulate CTC transport in the stenotic vessel. At this time, the irregular flow distribution caused by the inhomogeneous vessel shape greatly affects CTC adhesion. As shown in Figure 5B(i), CTCs were found to attach to vessel wall regions with lower wall shear stresses, i.e., stenotic corner region. The location and geometry distribution of CTC attachment to the vessel wall are in close agreement with the experimental data (Figure 5B(ii)). However, there is a slight difference between the CTC adhesion rate of the experiment and the simulation result, which can be related to the complex vascular surface conditions and stochastic nature of the CTC adhesion.

In Vitro Modeling on Extravasation of CTCs Adhered on Vessels into the Local Extracellular Matrix Environment. To study extravasation on our chips, model CTCs (PC3 cells) were perfused into the HUVEC-coated channel,

settled down, and adhered to the vessel lumen (Figure 6A, B). Then, the HGF-supplemented medium was loaded through

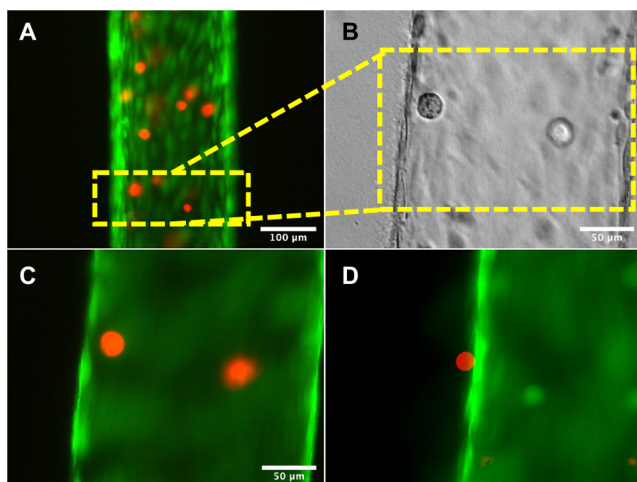


Figure 6. On-chip modeling the extravasation of tumor cells from the vessel tube toward the surrounding matrix. The vessel tube was labeled with CellTracker green, and the CTCs were stained with CellTracker red. (A) Representative fluorescent images of adhered CTCs on the vessel after perfusion. (B) Brightfield image of the CTC about to extravasate the vessel. (C) Fluorescent images of the CTC about to extravasate the vessel. (D) CTC extravasated across the vessel wall under HGF stimulation in 10 h. The scale bar for (A) is 100 μ m, and the ones for (B–D) are 50 μ m.

the side gel loading port via a pipet tip. Consequently, the CTC was activated and attracted toward the surrounding matrix outside the vessel without visibly disrupting the integrity of the vascular endothelium layer (Figure 6C, D). The process of CTC out-migration is observed to be similar to that reported for stem cell angiogenesis.⁴⁵ This may suggest that there is also mutual recognition between CTCs and vascular endothelial cells at the molecular level. Interestingly, the way CTCs extravasate blood vessels appeared to be related to their original density. The CTC cluster's trans-vessel migration was more brutal and faster, and they also destroyed the integrity of the vessels (Figure S4).

Unlike the slow effects of biochemical factors, such as cytokine and growth factor, on tumor growth, the effects of blood flow mechanics on the CTC transport process are dynamic and transient, making *in vivo* observations challenging. Our adaptable vessel-on-a-chip platform provides a high-fidelity biomimetic model for *in vitro* investigating several essential events involved in cancer metastasis, including tumor cell intravasation, CTC vascular transportation, and extravasation across the vessel. By reconstructing assorted tumor microenvironments and vessels with physiologically relevant sizes and geometries, corresponding CTC–vessel interactions can be recapitulated on-chip. In particular, we illustrated the impact of some mechano-physiological factors on CTC vascular transportation, such as VGCX and vessel geometry-induced hemodynamics. We demonstrated that both the VGCX shedding and stenotic vessel shape-induced disturbed flow could significantly increase CTC homing to the local vascular tissue. Combined with predictive computational flow simulations, we manifest a fluent methodology to interrogate biophysical clues in metastatic transport. Allowing accurate control of biophysiological and biomechanical parameters of the vessel–tumor model, our platform can be a practical tool for systematic dissection of metastasis mechanisms and screening of promising anticancer therapeutic candidates.

ASSOCIATED CONTENT

Supporting Information

The Supporting Information is available free of charge at <https://pubs.acs.org/doi/10.1021/acs.analchem.2c02556>.

Detailed experimental methods including microfluidic device fabrication, cell culture, vessel and related microenvironment constructions, and simulation (PDF)

Movie S: CTCs rolling on the vessel surface (AVI)

AUTHOR INFORMATION

Corresponding Author

Yaling Liu — Department of Bioengineering and Department of Mechanical Engineering and Mechanics, Lehigh University, Bethlehem, Pennsylvania 18015, United States;
Email: yal310@lehigh.edu

Authors

Yue Wu — Department of Bioengineering, Lehigh University, Bethlehem, Pennsylvania 18015, United States;  orcid.org/0000-0002-6564-2093

Yuyuan Zhou — Department of Bioengineering, Lehigh University, Bethlehem, Pennsylvania 18015, United States

Ratul Paul — Department of Mechanical Engineering and Mechanics, Lehigh University, Bethlehem, Pennsylvania 18015, United States

Xiaochen Qin — Department of Bioengineering, Lehigh University, Bethlehem, Pennsylvania 18015, United States

Khayrul Islam — Department of Mechanical Engineering and Mechanics, Lehigh University, Bethlehem, Pennsylvania 18015, United States

Complete contact information is available at:
<https://pubs.acs.org/10.1021/acs.analchem.2c02556>

Author Contributions

Y.L. conceived and supervised the study. Y.W., Y.Z., and Y. L. designed and performed the experiments. Y.W. collected and analyzed the data. Y.Z. assisted with data analysis. R.P. and K.I. assisted with computational model development. X.Q. assisted with figure edits. Y.W. wrote the manuscript. Y.Z., R.P., X.Q., K.I., and Y.L. revised the manuscript. All authors discussed the results and approved the submission.

Notes

The authors declare no competing financial interest.

ACKNOWLEDGMENTS

This work was supported by National Institute of Health Grant R01HL131750, R21EB033102, National Science Foundation Grant CBET 2039310, Pennsylvania Department of Health Commonwealth Universal Research Enhancement Program (CURE), and Pennsylvania Infrastructure Technology Alliance (PITA). We thank Mr. Anthony L. Jeffers for his help with microfabrication in the clean room.

REFERENCES

- (1) Siegel, R. L.; Miller, K. D.; Fuchs, H. E.; Jemal, A. *CA Cancer J. Clin.* **2021**, *71* (1), 7–33.
- (2) Lin, D.; Shen, L.; Luo, M.; Zhang, K.; Li, J.; Yang, Q.; Zhu, F.; Zhou, D.; Zheng, S.; Chen, Y.; Zhou, J. *Signal Transduct Target Ther* **2021**, *6* (1), 404.
- (3) Huang, Y.; Wang, S.; Guo, Q.; Kessel, S.; Rubinoff, I.; Chan, L. L.-Y.; Li, P.; Liu, Y.; Qiu, J.; Zhou, C. *Cancer Res.* **2017**, *77* (21), 6011–6020.
- (4) Wang, S.; Zhou, Y.; Qin, X.; Nair, S.; Huang, X.; Liu, Y. *Sci. Rep.* **2020**, *10* (1), 12226.
- (5) Teng, Y.; Xie, X.; Walker, S.; White, D. T.; Mumm, J. S.; Cowell, J. K. *BMC Cancer* **2013**, *13*, 453.
- (6) Sontheimer-Phelps, A.; Hassell, B. A.; Ingber, D. E. *Nat. Rev. Cancer* **2019**, *19* (2), 65–81.
- (7) Ao, Z.; Cai, H.; Wu, Z.; Krzesniak, J.; Tian, C.; Lai, Y. Y.; Mackie, K.; Guo, F. *Anal. Chem.* **2022**, *94* (2), 1365–1372.
- (8) Tao, T.; Deng, P.; Wang, Y.; Zhang, X.; Guo, Y.; Chen, W.; Qin, J. *Adv. Sci. (Weinh.)* **2022**, *9* (5), e2103495.
- (9) Brandenberg, N.; Hoehnel, S.; Kuttler, F.; Homicsko, K.; Ceroni, C.; Ringel, T.; Gjorevski, N.; Schwank, G.; Coukos, G.; Turcatti, G.; Lutolf, M. P. *Nat. Biomed. Eng.* **2020**, *4* (9), 863–874.
- (10) Hu, Z.; Cao, Y.; Galan, E. A.; Hao, L.; Zhao, H.; Tang, J.; Sang, G.; Wang, H.; Xu, B.; Ma, S. *ACS Biomater. Sci. Eng.* **2022**, *8* (3), 1215–1225.
- (11) Wu, Z.; Chen, B.; Wu, Y.; Xia, Y.; Chen, H.; Gong, Z.; Hu, H.; Ding, Z.; Guo, S. *Lab Chip* **2021**, *21*, 3498.
- (12) Wu, Y.; Zhou, Y.; Qin, X.; Liu, Y. *Biomicrofluidics* **2021**, *15* (6), 061503.
- (13) Wan, Z.; Kamm, R. D. *Nat. Biomed. Eng.* **2019**, *3* (6), 423–424.
- (14) Nagaraju, S.; Truong, D.; Mouneimne, G.; Nikkhah, M. *Adv. Healthc. Mater.* **2018**, *7* (9), 1701257.
- (15) Silvestri, V. L.; Henriet, E.; Linville, R. M.; Wong, A. D.; Pearson, P. C.; Ewald, A. J. *Cancer Res.* **2020**, *80* (19), 4288–4301.

- (16) Mollica, H.; Palomba, R.; Primavera, R.; Decuzzi, P. *ACS Biomater. Sci. Eng.* **2019**, *5* (9), 4834–4843.
- (17) Wong, A. D.; Searson, P. C. *Cancer Res.* **2014**, *74* (17), 4937–4945.
- (18) Zhang, Q.; Liu, T.; Qin, J. *Lab Chip* **2012**, *12* (16), 2837.
- (19) Goetz, J. G. *Science* **2018**, *362* (6418), 999–1000.
- (20) Mandrycky, C.; Hadland, B.; Zheng, Y. *Sci. Adv.* **2020**, *6* (38), eabb3629.
- (21) Buchanan, C. F.; Voigt, E. E.; Szot, C. S.; Freeman, J. W.; Vlachos, P. P.; Rylander, M. N. *Tissue Eng. Part C Methods* **2014**, *20* (1), 64–75.
- (22) Mitchell, M. J.; King, M. R. *Front. Oncol.* **2013**, *3*, 44.
- (23) Follain, G.; Herrmann, D.; Harlepp, S.; Hyenne, V.; Osmani, N.; Warren, S. C.; Timpson, P.; Goetz, J. G. *Nat. Rev. Cancer* **2020**, *20* (2), 107–124.
- (24) Ayuso, J. M.; Gong, M. M.; Skala, M. C.; Harari, P. M.; Beebe, D. J. *Adv. Healthc. Mater.* **2020**, *9* (3), 1900925.
- (25) Chen, B.; Wu, Y.; Ao, Z.; Cai, H.; Nunez, A.; Liu, Y.; Foley, J.; Nephew, K.; Lu, X.; Guo, F. *Lab Chip* **2019**, *19* (10), 1755–1763.
- (26) Virumbrales-Muñoz, M.; Ayuso, J. M.; Loken, J. R.; Denecke, K. M.; Rehman, S.; Skala, M. C.; Abel, E. J.; Beebe, D. J. *Biomaterials* **2022**, *283*, 121454.
- (27) Pauty, J.; Usuba, R.; Cheng, I. G.; Hespel, L.; Takahashi, H.; Kato, K.; Kobayashi, M.; Nakajima, H.; Lee, E.; Yger, F.; Soncin, F.; Matsunaga, Y. T. *EBioMedicine* **2018**, *27*, 225–236.
- (28) Chen, Y.-C.; Allen, S. G.; Ingram, P. N.; Buckanovich, R.; Merajver, S. D.; Yoon, E. *Sci. Rep.* **2015**, *5* (1), 9980.
- (29) Azevedo, A. S.; Follain, G.; Patthabhiraman, S.; Harlepp, S.; Goetz, J. G. *Cell Adh. Migr.* **2015**, *9* (5), 345–356.
- (30) van Dijk, C. G. M.; Brandt, M. M.; Pouli, N.; Anten, J.; van der Moolen, M.; Kramer, L.; Homburg, E. F. G. A.; Louza-Martinez, L.; Pei, J.; Krebber, M. M.; van Balkom, B. W. M.; de Graaf, P.; Duncker, D. J.; Verhaar, M. C.; Luttge, R.; Cheng, C. *Lab Chip* **2020**, *20* (10), 1827–1844.
- (31) Chiang, S. P. H.; Cabrera, R. M.; Segall, J. E. *Am. J. Physiol. Cell Physiol.* **2016**, *311* (1), C1–C14.
- (32) Scarpino, S.; Stoppacciaro, A.; Colarossi, C.; Cancellario, F.; Marzullo, A.; Marchesi, M.; Biffoni, M.; Comoglio, P. M.; Prat, M.; Ruco, L. P. *J. Pathol.* **1999**, *189* (4), 570–575.
- (33) Xia, P.; Gamble, J. R.; Rye, K. A.; Wang, L.; Hii, C. S.; Cockerill, P.; Khew-Goodall, Y.; Bert, A. G.; Barter, P. J.; Vadas, M. A. *Proc. Natl. Acad. Sci. U. S. A.* **1998**, *95* (24), 14196–14201.
- (34) Mollica, H.; Coclico, A.; Miali, M. E.; Pereira, R. C.; Palleari, L.; Manneschi, C.; DeCensi, A.; Decuzzi, P. *Biomicrofluidics* **2018**, *12* (4), 042205.
- (35) Weinbaum, S.; Tarbell, J. M.; Damiano, E. R. *Annu. Rev. Biomed. Eng.* **2007**, *9* (1), 121–167.
- (36) Le Bras, G. F.; Taubenslag, K. J.; Andl, C. D. *Cell Adh. Migr.* **2012**, *6* (4), 365–373.
- (37) Pahakis, M. Y.; Kosky, J. R.; Dull, R. O.; Tarbell, J. M. *Biochem. Biophys. Res. Commun.* **2007**, *355* (1), 228–233.
- (38) Hynes, W. F.; Pepona, M.; Robertson, C.; Alvarado, J.; Dubbin, K.; Triplett, M.; Adorno, J. J.; Randles, A.; Moya, M. L. *Sci. Adv.* **2020**, *6* (35), eabb3308.
- (39) Rehm, M.; Bruegger, D.; Christ, F.; Conzen, P.; Thiel, M.; Jacob, M.; Chappell, D.; Stoeckelhuber, M.; Welsch, U.; Reichart, B.; Peter, K.; Becker, B. F. *Circulation* **2007**, *116* (17), 1896–1906.
- (40) Wang, G.; Kostidis, S.; Tiemeier, G. L.; Sol, W. M. P. J.; de Vries, M. R.; Giera, M.; Carmeliet, P.; van den Berg, B. M.; Rabelink, T. J. *Arterioscler. Thromb. Vasc. Biol.* **2020**, *40* (2), 350–364.
- (41) Tovar-Lopez, F.; Thurgood, P.; Gilliam, C.; Nguyen, N.; Pirogova, E.; Khoshmanesh, K.; Baratchi, S. *Front. Bioeng. Biotechnol.* **2019**, *7*, 81.
- (42) Papaioannou, T. G.; Stefanadis, C. *Hellenic J. Cardiol.* **2005**, *46* (1), 9–15.
- (43) Chen, M. B.; Whisler, J. A.; Fröse, J.; Yu, C.; Shin, Y.; Kamm, R. D. *Nat. Protoc.* **2017**, *12* (5), 865–880.
- (44) Ayachit, U.; Avila, L. S.; Bauer, A.; Boeckel, B.; Aashish, C.; DeMarle, D.; Geveci, B.; Jordan, S.; Loring, B.; Maxwell, T.;
- McKenzie, S.; Moreland, K.; Osterdahl, K.; Patchett, J.; Quammen, C.; Waldon, S.; Zagaris, G. *ParaView Guide: A Parallel Visualization Application*; Kitware, Inc., 2015.
- (45) Allen, T. A.; Gracieux, D.; Talib, M.; Tokarz, D. A.; Hensley, M. T.; Cores, J.; Vandergriff, A.; Tang, J.; de Andrade, J. B. M.; Dinh, P.-U.; Yoder, J. A.; Cheng, K. *Stem Cells* **2017**, *35* (1), 170–180.

□ Recommended by ACS

Verification and Analysis of Filter Paper-Based Intracellular Delivery of Exogenous Substances

Guorui Zhang, Jinyi Wang, et al.

JANUARY 09, 2023

ANALYTICAL CHEMISTRY

READ ▾

Organ-on-a-Chip Platform with an Integrated Screen-Printed Electrode Array for Real-Time Monitoring Trans-Epithelial Barrier and Bubble Formation

Akshay Krishnakumar, Rahim Rahimi, et al.

FEBRUARY 10, 2023

ACS BIOMATERIALS SCIENCE & ENGINEERING

READ ▾

Multiplex Digital Polymerase Chain Reaction on a Droplet Array SlipChip for Analysis of KRAS Mutations in Pancreatic Cancer

Qixin Hu, Feng Shen, et al.

DECEMBER 15, 2022

ACS SENSORS

READ ▾

Microvessel-on-Chip Fabrication for the In Vitro Modeling of Nanomedicine Transport

Sergio Dávila, Isabel Rodríguez, et al.

SEPTEMBER 23, 2021

ACS OMEGA

READ ▾

Get More Suggestions >